



## Transition from electron-dominated to phonon-driven thermal transport in tungsten under extreme pressures

Niraj Bhatt , Pravin Karna, Sandip Thakur , and Ashutosh Giri\*

*Department of Mechanical, Industrial and Systems Engineering, University of Rhode Island, Kingston, Rhode Island 02881, USA*



(Received 28 July 2023; revised 15 September 2023; accepted 17 October 2023; published 8 November 2023)

By utilizing a combination of first-principles calculations and machine-learning-interatomic-potential-based molecular dynamics simulations, we show that (contrary to the conventional understanding of electron-driven thermal transport in metals) the dominant carriers of heat in tungsten are phonons at high pressures. More specifically, we show that the contribution of phonons to the total thermal conductivity increases monotonically from  $\sim 30\%$  at ambient pressure to  $\sim 70\%$  at 100 GPa. This is attributed to considerable phonon hardening leading to enhanced phonon lifetimes and group velocities in pressurized tungsten. In contrast to the phonon-driven thermal conductivity, calculations of the electronic thermal conductivity based on density functional perturbation theory calculations of the full electron-phonon coupling matrix show that there is negligible change in the electron-driven thermal conductivity throughout the entire pressure range (up to 100 GPa) studied in this paper. Spectrally resolved electron-phonon coupling at elevated pressures reveals that while phonons are hardened, the peaks of the spectral function are unchanged, thus resulting in negligible variation of the mass enhancement parameter that describes the strength of the overall electron-phonon coupling with increasing pressures. In contrast, the characteristically reduced phonon-phonon scattering, a signature of the isotropic and highly degenerate phonon branches, leads to the phonon-dominated heat conduction in pressurized tungsten. Taken together, our results show that the pressure-driven changes in thermal transport can result in large deviations of the Lorenz number from the traditionally accepted Sommerfeld value in tungsten. Our work reveals an efficient way to separately manipulate the phononic thermal transport from the electronic heat conduction through the application of external pressure in tungsten, and as such can be highly beneficial for applications such as in integrated circuits where tungsten could replace the widely used copper interconnects.

DOI: [10.1103/PhysRevMaterials.7.115001](https://doi.org/10.1103/PhysRevMaterials.7.115001)

### I. INTRODUCTION

It has been well documented and conventionally accepted that free electrons are the dominant carriers of both charge and heat in elemental metals [1]. As a consequence, the ratio between the thermal ( $\kappa$ ) and electronic conductivity ( $\sigma$ ) is approximately constant at an absolute temperature; that is, the Lorenz number,  $L = \kappa/\sigma T$  for several elemental metals is typically very close to the Sommerfeld value of  $L_0 = \pi^2 k_B^2/3e^2 = 2.44 \times 10^{-8} \text{ W } \Omega \text{ K}^{-2}$  [2]. The physical meaning of this universal constant (also commonly referred to as the Wiedemann-Franz law) [3] is that the largest contribution to the heat conduction is through the same free electrons that transfer electric current in metals. However, the predictions of the Wiedemann-Franz law can substantially deviate from experimental measurements of the thermal conductivity in metals if there is a non-negligible contribution from the lattice to their overall thermal conductivity. Although, for complex metallic alloys, the Wiedemann-Franz law in conjunction with the measurement of the electrical conductivity and total thermal conductivity has been utilized to elucidate the lattice contribution, for elemental metals the lattice contribution typically has negligible influence on the total thermal conductivity [4].

With the recent advancements in computational frameworks that can now accurately quantify the interactions between all phonon modes and electronic eigenstates fully from first principles [5–7], considerable contributions from the lattice to the total thermal conductivity have been identified for several elemental metals [4,8]. For example, as much as 30% of heat conduction under ambient conditions in tungsten has been ascribed to phonons [8], thus explaining its departure from the widely accepted Wiedemann-Franz law. The reason for this disagreement was long (incorrectly) thought to originate from the complex band structure of transition metals [9,10], since computational frameworks capable of untangling the phonon contributions resulting from the coupled electron-phonon and phonon-phonon interactions were not yet available. However, with the recent advancements in parameter-free density functional theory (DFT) calculations, as we discuss in more detail below, it has now become possible to investigate the electronic and phononic contributions to comprehensively understand their separate influences on the overall heat transfer processes. This raises the question, Can the newly formulated understanding be utilized to control the electron and phonon contributions separately? Going one step further, can we engineer the phonon contribution to surpass the electronic contribution in metals? This not only would be vital in terms of our understanding of condensed matter but also would be important from an applicative standpoint where manipulating and processing heat flow through

\*ashgiri@uri.edu

untangling the dynamics of individual energy carriers can potentially be highly beneficial, for instance, in nanointerconnects where continued miniaturization has led to severe size effects [11–13]. Herein, utilizing the recent advancements in the computational process to accurately (and separately) calculate the phononic ( $\kappa_p$ ) and electronic ( $\kappa_e$ ) contributions to the total thermal conductivity, we will comprehensively show that the lattice contribution can be monotonically increased (by up to 70% of the overall thermal conductivity) under extreme pressure conditions (of up to 100 GPa) leading to the strong departure of the Lorenz number from the Sommerfeld value in pressurized tungsten.

In general, high-pressure studies have provided critical insights into novel physical phenomena that are otherwise masked under ambient conditions [14]. For instance, high-pressure studies have been utilized to increase the superconducting transition temperature in metals that are not superconducting under ambient conditions [15–17], modulate the thermal conductivity of solids across a wide range [18–21], and enhance interfacial thermal conductance between two solids by stiffening the interfacial bonding [22–24]. With regard to understanding the fundamental dynamics of energy carriers at high pressures, first-principles-based studies have shown that phonon-phonon scattering rates can either increase or decrease depending on the phase space available for acoustic phonons (which are the dominant heat carriers) in nonmetallic, semiconducting crystals far from their pressure-induced phase transitions [25–27]. Similarly, *ab initio* calculations on metals have shown that the application of hydrostatic pressures can lead to either an increase or a decrease in the electron-phonon scattering rates depending on the type of the electronic band structure of the metal [16,28,29]. Thus these predictive studies based on first-principles calculations can lend significant insights into the fundamental dynamics and relaxation processes of the coupled energy states in condensed matter that are readily becoming accessible through diamond anvil cell experiments combined with pump-probe thermoreflectance spectroscopy, which are able to measure the thermal transport properties of materials under high-pressure conditions [20,21,24,30].

In terms of advancements in the theoretical description of the energy exchange between the electronic and vibrational states in metals, the early works by Kaganov *et al.* [31] Anisimov *et al.* [32], and Allen and co-workers [33–35], which were reliant on the two-temperature approach, and subsequent more robust theories based on first-principles calculations [29,36,37] have most notably shown that the energy transfer rate between the two subsystems is significantly enhanced at elevated electron temperatures. However, similar advancements in the description of electron-phonon relaxation rates in different metals under extreme pressure conditions have remained largely elusive [28,38]. This could partly be due to the fact that properly accounting for all phonon mode interactions with every electronic state in the entire Brillouin zone requires fine meshes of the electron and phonon wave vectors to accurately describe the physics at high pressures. For example, it has been shown that dense electron and phonon wave-vector grids are necessary to precisely resolve the fine features of the electron-phonon coupling to determine the superconducting transition temperatures in elemental metals [16,39]. In this

regard, recent developments in parameter-free first-principles-based calculations of electron-phonon scattering have enabled such calculations in dense wave-vector grids through Wannier functions that efficiently interpolate the complex band structures from coarser grids, thus making the calculations computationally more tractable [5,6,40]. Utilizing this recent advancement, several studies [4,7,38,41,42], including our works [28,43,44], have calculated the electron-driven thermal conductivity in elemental metals by solving the full Fermi's golden rule. These studies have elucidated critical insights into the spectral-level details of electron-phonon coupling, including mode-dependent phonon lifetimes that are limited by electron-phonon scattering [4,7].

For predicting phonon-driven thermal transport, significant advancements in first-principles-based calculations that solve the full Boltzmann transport equation (BTE) have considerably broadened our understanding of the phonon physics in several types of crystalline solids including metals and non-metals; the reader is referred to Refs. [45,46] for a detailed review of this topic. However, such approaches of solving the BTE based on force constants obtained from DFT calculations are either computationally cumbersome (since the DFT calculations must be performed on supercells with large number of atoms) or do not fully include higher-order interactions since these calculations are mostly limited to lowest-order interactions among three phonons [45]. Although calculations with higher-order four-phonon scattering processes requiring quartic force constants have also recently been performed for several materials [47–51], including such fourth-order anharmonic processes can dramatically increase the computational cost of the calculations. These higher-order processes, however, have been shown to have an opposing response at higher pressures as compared with three-phonon processes in some material systems such as in cubic boron arsenide [27]. Therefore, to correctly predict the phonon-driven thermal transport under pressurized conditions where phonon hardening generally leads to considerable broadening of the phonon spectrum to higher frequencies in solids, higher-order anharmonic scattering processes need to be incorporated while determining the phonon-phonon interactions for thermal transport calculations. In this regard, molecular dynamics (MD) simulations are preferred since they intrinsically account for the full anharmonicity of the atomic interactions given the appropriate choice of the interatomic potential to accurately describe the material system. As such, recent advancements in machine-learning-based (ML-based) interatomic potentials that are trained through data obtained from *ab initio* calculations can provide first-principles accuracies in describing the vibrational physics of solids [52–59]. This offers the prospect of performing large-scale simulations of thermal transport that inherently require large supercells with considerably lower computational costs as compared with solving the full BTE based on first principles, which is often computationally prohibitive, especially when considering higher-order processes.

In this paper, we utilize a combination of a ML-based interatomic potential for MD simulations and first-principles calculations of the full electron-phonon coupling matrix to comprehensively investigate the thermal transport mechanisms in pressurized tungsten. Our MD simulations under the Green-Kubo (GK) formalism predict a monotonically

increasing contribution of  $\kappa_p$  from 30% at ambient pressure to 70% under extreme pressure conditions of 100 GPa. Our MD simulations in conjunction with spectral energy density (SED) calculations show that the enhanced lattice contribution with pressure originates from considerable phonon hardening leading to increased phonon lifetimes and group velocities in pressurized tungsten. In contrast to this phonon-driven thermal conductivity, calculations of  $\kappa_e$  based on density functional perturbation theory (DFPT) calculations of the full electron-phonon coupling matrix show that there is negligible change in the electron-driven thermal conductivity throughout the entire pressure range (up to 100 GPa) studied in this paper. We attribute this to the negligible change in the overall electron-phonon coupling strength with pressure, which leads to minimal changes in the average electron lifetimes near the Fermi energy. Taken together, our results show that the pressure-driven changes in thermal transport can result in large deviations of the Lorenz number from the traditionally accepted Sommerfeld value. Our results can also help guide experiments towards separately controlling the phonon- and electron-driven thermal transport in tungsten.

## II. RESULTS AND DISCUSSION

Before discussing our thermal conductivity results, we first compare the phonon dispersions calculated from our machine learning potential (MLP) with our DFT calculations and experimental results taken from Ref. [60] as shown in the top panel of Fig. 1(a). Our MLP-based calculations agree very well with both the experimental results and our DFT calculations. Moreover, our mode-specific calculations of the electron-phonon coupling as shown in the bottom panel of Fig. 1(a) depicting the phonon linewidths,  $\gamma = \hbar/\tau$ , or the imaginary part of the phonon self-energy that is related to the lifetimes,  $\tau$ , of the individual phonon modes [61], show that the linewidths are much higher at the zone boundary along the  $\Gamma$ - $H$  direction with the ‘dip’ in the dispersion as highlighted in the bottom panel of Fig. 1(a). This dip is well captured by our MLP, and as such, the phonon dynamics predicted with our MLP captures key features of the phonon dispersion providing confidence in our use of the MLP-based MD simulations to predict the phonon contributions to thermal conductivity of tungsten as we discuss in detail below.

We first present the temperature-dependent thermal conductivity of unpressurized tungsten from room temperature to 1100 K in Fig. 1(b). Note that we study this intermediate temperature regime since electron-impurity and electron-electron scattering are less pronounced as compared with electron-phonon interactions, which primarily dictate the resistance to heat flow at these temperatures. Our calculations of the total thermal conductivity at room temperature that take into account both the electron and phonon contributions agree within 12% of the values reported in prior first-principles-based calculations [8,38]. Moreover, our MLP-based GK-predicted  $\kappa_p$  of  $60 \pm 9 \text{ W m}^{-1} \text{ K}^{-1}$  at room temperature also agrees very well with prior work that has calculated the phonon contribution to the total thermal conductivity by solving the BTE that includes three-phonon scattering processes [38].

The very high room temperature  $\kappa_p$  of W ( $60 \pm 9 \text{ W m}^{-1} \text{ K}^{-1}$ ) when compared with other elemental metals

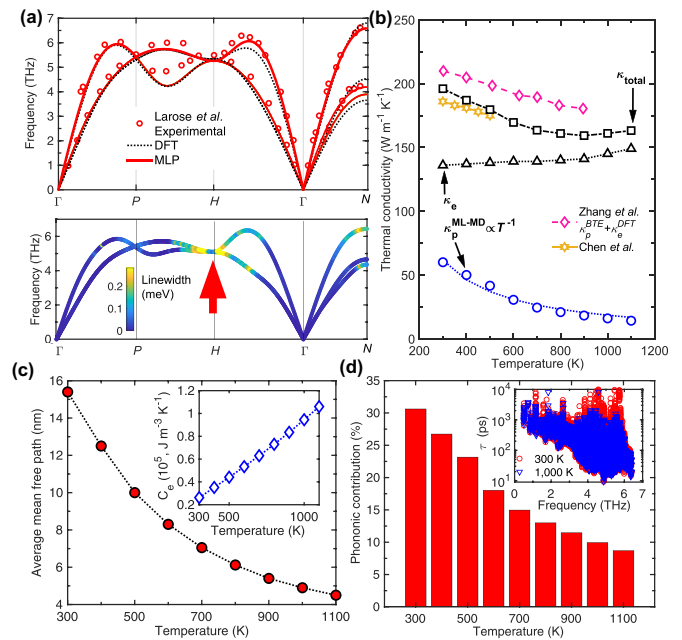


FIG. 1. (a) Machine-learning-potential-based calculations of the phonon dispersion of tungsten showing great agreement with the experimentally measured dispersion (given by Larose and Brockhouse [60]) and our density functional theory calculations (top panel). The machine learning potential can correctly capture the ‘dip’ in the phonon spectrum. At this dip, our calculations of the electron-phonon interactions show enhanced coupling associated with the specific phonon modes as quantified by the calculations of the phonon linewidths (bottom panel). As such, our machine learning potential captures such key features in the phonon dispersion. (b) Temperature-dependent thermal conductivity contributions from the electronic and phononic subsystems. While the electronic contributions increase, the phonon thermal conductivity shows a pronounced decrease with temperature due to anharmonic phonon-phonon scattering that increases with temperature. At room temperature, our results agree well with prior calculations from the BTE that considers three-phonon scattering processes as conducted by Chen *et al.* [8] and Zhang *et al.* [38]. (c) Average mean free paths of electrons near the Fermi level in tungsten as a function of temperature. Inset: electronic heat capacity as a function of temperature showing the monotonic increase with temperature. (d) Phononic contribution to total thermal conductivity as a function of temperature in tungsten. Inset: as temperature is increased, the electron-phonon-scattering-induced phonon lifetimes decrease slightly. Along with increased anharmonic phonon-phonon scattering, the slight increase in the electron-phonon scattering can also facilitate the reduction in the contributions from the lattice at higher temperatures.

such as Al, Ag, and Au (with  $\kappa_p$  values of 6, 4, and  $2 \text{ W m}^{-1} \text{ K}^{-1}$ , respectively) [7] is a consequence of the reduced anharmonic phonon-phonon scattering in tungsten [8,62]. This weak phonon-phonon scattering can be attributed to the degeneracy of the phonon branches [62]. For example, the phonon branches at the  $P$  and  $H$  points in the Brillouin zone for body-centered-cubic (bcc) structures show triple degeneracy [see Fig. 1(a)]. Another factor which separates the lattice dynamics of W from other bcc metals originates from its uniquely isotropic phonon dispersion as shown in Fig. 1. The transverse acoustic branches are degenerate along the

entire  $\Gamma$ - $P$ - $H$ - $\Gamma$  paths with degeneracy for all three branches at the  $P$  and  $H$  points [Fig. 1(a)]. Therefore the phase space available for phonon scattering is relatively small in tungsten as compared with other bcc metals with phonon branches that have a wider separation in frequencies at particular points in the Brillouin zone. The wider separation in frequencies and thus bigger phase space for phonon-phonon scattering increase the anharmonicity by opening up emission or absorption channels, which can lead to the reduction in the lattice thermal conductivity [7].

The agreement between our MLP MD-predicted room-temperature thermal conductivity of tungsten and the results from solving the BTE with three-phonon processes under ambient conditions suggests that higher-order processes (which are inherently included in MD simulations) do not significantly influence the lattice-driven thermal transport in tungsten. This is reinforced by the  $\kappa_p \propto T^{-1}$  dependence obtained from our MD simulations, which indicates the strong role of three-phonon anharmonic processes in dictating the temperature dependence of  $\kappa_p$  of tungsten in the 300–1100 K range.

In contrast to the decreasing  $\kappa_p$  with temperature, the electron-driven thermal conductivity increases monotonically across the entire temperature range as shown in Fig. 1(b). In the simple kinetic theory description of thermal transport, thermal conductivity is given as  $\kappa = (1/3)(Cv\Lambda)$ , where  $C$  is the heat capacity,  $v$  is the velocity, and  $\Lambda$  is the mean free path of the energy carriers. Although the average  $\Lambda$  of electrons at the Fermi level decreases with increasing temperature while the Fermi velocity remains constant, the heat capacity of electrons increases by more than a factor of 4 when temperature is increased from room temperature up to 1100 K [inset of Fig. 1(c)]. This leads to the monotonically increasing electron thermal conductivity with temperature and also results in the dominant role of electrons in the total thermal conductivity in unpressurized tungsten. Taken together with the decreasing trend in the lattice thermal conductivity due to increasing anharmonic effects, the phonon contribution decreases to  $\sim 8\%$  at 1100 K [Fig. 1(d)]. Along with the increase in anharmonic phonon-phonon scattering, the electron-phonon scattering also increases with temperature (albeit much less dramatically for the temperature range studied), thus slightly reducing the phonon lifetimes,  $\tau$ , as shown in the inset of Fig. 1(d). Note that although the increase in the scattering rate of electrons due to electron-phonon interactions with temperature is more pronounced (see Fig. S11 of the Supplemental Material [63]), the increase in the electronic heat capacity compensates for the decrease in electron lifetime. Consequently, the contrasting temperature trends between the two subsystems ultimately result in the decrease of the total thermal conductivity with increasing temperatures (which is in agreement with prior results) [8,38]. Next, we consider the effect of pressure on the electronic- and lattice-driven thermal transport in tungsten. As shown in Fig. 2(a), the total thermal conductivity of tungsten increases monotonically from  $\sim 200 \text{ W m}^{-1} \text{ K}^{-1}$  at ambient pressure to  $\sim 505 \text{ W m}^{-1} \text{ K}^{-1}$  at 100 GPa. This increase can mainly be ascribed to the enhanced phonon contributions, whereby  $\kappa_p$  increases more than fourfold while the increase in  $\kappa_e$  is not as substantial. Thus the application of pressure raises the phononic contribution to the total thermal conductivity from  $\sim 30\%$  at ambient pressure to almost 70% at

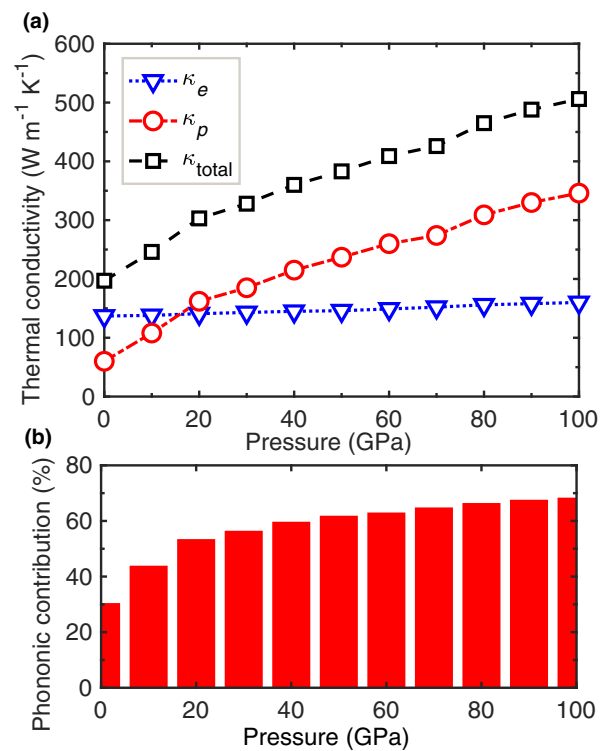


FIG. 2. (a) Contributions from phonons and electrons to the total thermal conductivity of tungsten as a function of pressure. While the electron thermal conductivity has negligible change with pressure, the phonon-driven thermal conductivity increases monotonically. (b) The phonon contribution to the total thermal conductivity increases from  $\sim 30\%$  to  $\sim 70\%$  with pressures increasing from ambient pressure to 100 GPa.

100 GPa [Fig. 2(b)]. In what follows, we will attempt to better understand the contrasting responses from the electronic and phononic subsystems under high-pressure conditions in tungsten, which shows a unique transition (away from any phase transitions) from an electron-driven heat conduction to a phonon-driven heat conduction as pressure is increased.

The application of pressures of up to 100 GPa is shown to considerably stiffen the lattice leading to phonon hardening (Fig. S17) [63]. As mentioned above and explored in more detail in the following analyses, although the effect of this hardening has significant influence on the phononic heat conduction,  $\kappa_e$  has a less pronounced effect. This has its origins in the pressure dependence (or the lack thereof) of the mass enhancement parameter,  $\lambda = 2 \int_0^\infty (\alpha^2 F(\omega)/\omega) d\omega$ , that describes the strength of electron-phonon coupling in tungsten as shown in Fig. 3(a). Here,  $\alpha^2 F(\omega)$  is the Eliashberg spectral function, and  $\omega$  is the phonon frequency. For comparison, we also include  $\lambda$  values for three other metals (calculated with a similar parameter-free first-principles approach) from our prior work in Ref. [28]. While the pressure dependencies of  $\lambda$  for Al, Au, and Ag reduce considerably with increasing pressure,  $\lambda$  for W shows negligible change with pressure. Considering their respective electronic densities of states (eDOSs), it becomes evident that the transition metal (W) has a completely different eDOS around the Fermi level as compared with the free-electron metals (Al, Au, and Ag) with

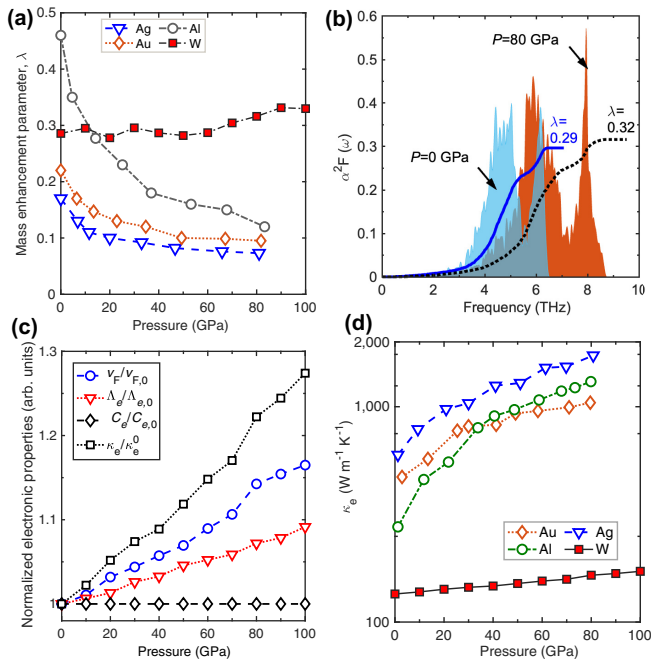


FIG. 3. (a) Mass enhancement parameter,  $\lambda$ , describing the strength of electron-phonon coupling as a function of pressure for tungsten. For comparison, we also include the calculations for free-electron-like metals (Al, Au, and Ag) taken from Ref. [28]. (b) The Eliashberg spectral function for tungsten at 0 and 80 GPa pressures. Although the phonon spectrum broadens with pressure, the peaks in the spectral function do not vary drastically, which results in similar values of  $\lambda$  across the entire pressure range as shown in (a). (c) The average Fermi velocity and the average mean free paths at the Fermi level increase monotonically with pressure, while the electronic heat capacity has a negligible change. This leads to a monotonically increasing electronic thermal conductivity that increases by  $\sim 25\%$  at 100 GPa. (d) Comparison of electron thermal conductivity of tungsten as a function of pressure with the free-electron-like metals [28]. While the electronic thermal conductivity increases drastically with pressure for the free-electron metals, for tungsten the increase is not that pronounced since the electron-phonon coupling strength has negligible variations with pressure as shown in (a).

the relatively flat eDOS around the Fermi level (Fig. S18) [63]. Moreover, while the eDOS at the Fermi level is lowered monotonically for the free-electron-like metals with increasing pressure, for W the eDOS does not vary significantly with pressure at the Fermi level (Fig. S19) [63].

As shown in Fig. 3(b), our calculations of the electron-phonon spectral functions,  $\alpha^2 F(\omega)$ , under ambient and 80 GPa pressure conditions show that although phonon hardening leads to the broadening of the spectral function to higher phonon frequencies, the height of the peaks in the spectral function has negligible change with pressure. As a consequence, the calculation of the overall electron-phonon coupling strength [ $\lambda = 2 \int_0^\infty (\alpha^2 F(\omega)/\omega) d\omega$ ] does not significantly change for W as compared with the free-electron-like metals [28]. As such, the average mean free paths of electrons around the Fermi level only increase by up to 10% at 100 GPa pressure [Fig. 3(c)]. Moreover, we also find that the heat capacity of electrons has negligible change with pressure

(Fig. S8) [63] while the Fermi velocity increases by  $\sim 15\%$ , whereby it monotonically increases from  $\sim 0.94 \times 10^6$  m/s at ambient pressure to  $\sim 1.13 \times 10^6$  m/s at 100 GPa (Fig. S9) [63]. Therefore, as shown in Fig. 3(c),  $\kappa_e$  shows a modest and monotonic increase by  $\sim 1.25$  times across the entire range of pressure studied in this paper. This is in contrast to the relatively higher increases in  $\kappa_e$  of the free-electron-like metals [Fig. 3(d)] [28], which highlights the important role of the electronic band structure in dictating the pressure response of the electronic heat conduction in elemental metals.

We now turn our focus to the increasing role of the phonon-driven thermal transport in tungsten with increasing pressures. To gain more insight into this, we perform SED calculations to understand the variations in the phonon-mode-specific properties with the application of high pressures. Briefly, the SED calculations can unravel the anharmonic phonon dispersions and lifetimes of individual phonon modes [64]. In the absence of anharmonic interactions between vibrational modes, assuming a purely harmonic system, the evaluation of the SED would precisely reproduce the harmonic phonon dispersion. However, anharmonic effects become evident through a broadening of the SED profiles and an increase in the contrast in shading. Thus the higher contrast in the shading (or the higher magnitude of the SEDs) represents increased anharmonicities of those modes. As shown in Fig. 4(a), high-frequency modes in tungsten possess higher SEDs at ambient and high pressures, especially at the Brillouin zone edge. This is consistent with broadened linewidths of phonon modes due to enhanced electron-phonon interactions highlighted in the bottom panel of Fig. 1(a) at the “dip” in the phonon dispersion (which is at the  $H$  point in the Brillouin zone).

From our SED calculations, we calculate higher phonon lifetimes across the entire phonon spectrum in tungsten with the application of high pressures as shown in Fig. 4(b). For comparison, we also plot the phonon lifetimes that we calculate for silicon, which is a prototypical semiconductor with high lattice thermal conductivity. Even at high pressures, the phonon lifetimes in tungsten are comparably much narrower with respect to the broader spectrum in silicon involving higher-frequency modes. Furthermore, the phonon lifetimes in silicon are much higher than in unpressurized tungsten throughout the phonon spectrum. However, for pressurized tungsten [as shown for the 80-GPa case in Fig. 4(b)], the phonon lifetimes are more comparable to those of silicon, and this helps explain the high phonon thermal conductivity (which is comparable to the thermal conductivity of silicon) [65] which we calculate for pressurized tungsten with our MLP-based MD simulations. Note that although silicon is a semiconductor where electron-phonon coupling plays a negligible role at room temperature, the comparison is mainly to highlight that the phonon lifetimes in tungsten (an elemental metal) can be engineered to approach that of a semiconductor with a high lattice-driven thermal conductivity. Furthermore, the application of pressure increases the slope of the phonon branches, thus leading to higher group velocities for phonons across the entire spectrum with increasing pressure [Fig. 4(c)]. Therefore both the increase in phonon group velocities and the increase in phonon lifetimes lead to the monotonically increasing  $\kappa_p$  in tungsten with the application of pressure.

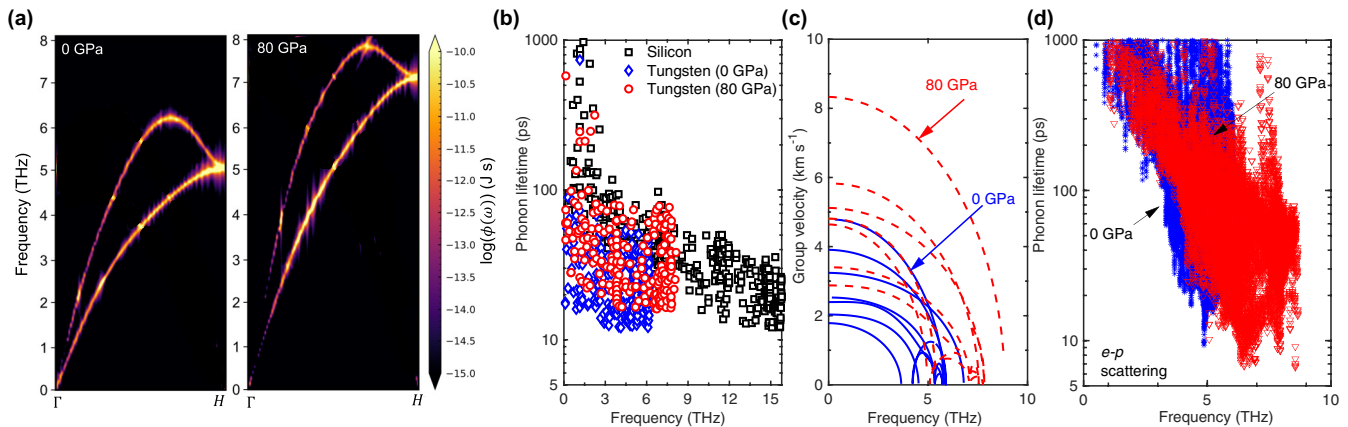


FIG. 4. (a) Spectral energy density calculations under ambient and 80 GPa pressure conditions. (b) Phonon lifetimes obtained from the SED calculations show an increase with pressure in tungsten. At high pressures, the phonon lifetimes in tungsten are comparable to those of silicon, a semiconducting material with high lattice thermal conductivity. (c) Phonon group velocities also increase with increasing pressures as shown for the cases of 0 and 80 GPa. (d) Phonon lifetimes due to electron-phonon (e-p) interactions in tungsten at 0 and 80 GPa pressures. Although the lifetimes of the low-frequency phonons are almost an order of magnitude higher than the lifetimes obtained from our SED calculations, the lifetimes for higher-frequency phonons ( $> 5$  THz) are comparable to our SED calculations.

It is also interesting to note that the phonon lifetimes of the lower-frequency modes are mainly dictated by phonon-phonon scattering since the electron-phonon-scattering-based lifetimes are almost an order of magnitude of higher [Fig. 4(d)]. Only for higher frequencies does electron-phonon scattering lead to a significant reduction in their lifetimes. This is also clear from the phonon linewidths presented in the bottom panel of Fig. 1(a) for the 0-GPa case (and Fig. S23 for the 80-GPa case) [63], where electron-phonon scattering mainly affects the higher-frequency phonon modes at the Brillouin zone edge, especially near the “dip” at the  $H$  point. For the lower-frequency phonons, although phonon-phonon scattering dictates their lifetimes as compared with electron-phonon scattering, from the phonon dispersions at the various pressures, it is also evident that the isotropic nature and the high degree of degeneracy of the phonon branches in tungsten result in phonon lifetimes that are comparable to those in silicon due to reduced phonon-phonon scattering. In fact, from harmonic calculations we find that the phase space (for three-phonon scattering in the lower-frequency region) is reduced with the application of pressure and, in comparison to a more anharmonic metal such as gold, the phase space for scattering in tungsten is considerably reduced (Fig. S22) [63]. Therefore, along with the increase in phonon lifetimes and group velocities, the application of extreme pressures (of up to 100 GPa) results in a monotonic increase in the contribution from the lattice to the total thermal conductivity from  $\sim 30\%$  at ambient pressure to  $\sim 70\%$  at 100 GPa for tungsten. We note that our result of increasing phonon thermal conductivity with pressure is in disagreement with the pressure-independent lattice thermal conductivity for W predicted from first-principles-based BTE calculations including three-phonon interactions in Ref. [38]. The pressure independence was argued to originate from the lower transverse acoustic phonon branches along the  $\Gamma$ - $N$  direction becoming relatively softer than other branches under pressure, thus increasing the phase space for scattering. Our calculations do not show such differences in the pressure response

of the phonon branches, where the isotropic nature of the phonon dispersion is still preserved under high-pressure conditions (see Fig. S22) [63]. Thus the phase space for scattering does not increase in our calculations, and therefore we do not observe pronounced phonon-phonon scattering at higher pressures as was conjectured in Ref. [38].

Finally, we discuss the influence of pressure on the Lorenz number in tungsten. Figure 5 shows the ratio of the calculated Lorenz number based on our total thermal conductivity to the Sommerfeld value ( $L_{\text{total}}/L_0$ ) and the ratio of the electronic thermal conductivity to the Sommerfeld value ( $L_e/L_0$ ). A value of unity represents the scenario where the mean free

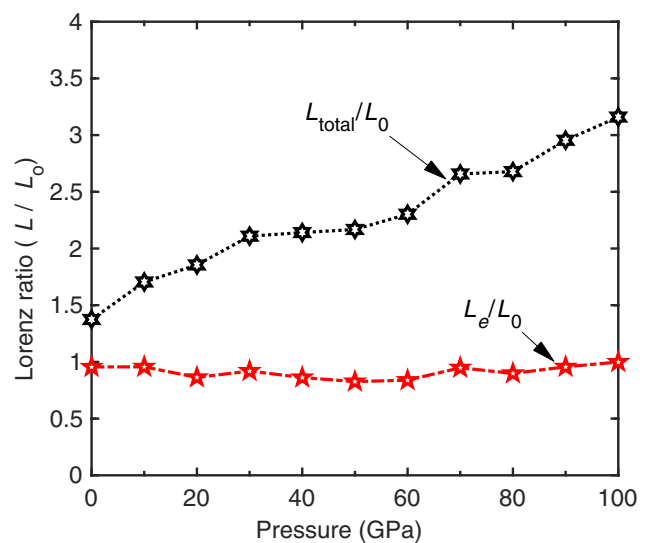


FIG. 5. Ratio of the Lorenz number based on the total thermal conductivity to the Sommerfeld value ( $L_{\text{total}}/L_0$ ) and the ratio of the electronic thermal conductivity to the Sommerfeld value ( $L_e/L_0$ ). The Lorenz number calculated based on the total thermal conductivity deviates considerably from the Sommerfeld value with increasing pressure and is more than  $3 \times L_0$  at 100 GPa pressure.

paths of free electrons for heat and charge conduction are the same. Not surprisingly, the ratio of the electronic part ( $L_e$ ) to the Sommerfeld value does not deviate from unity for the entire pressure range. However, for the ratio involving the total thermal conductivity considering both the phonon and electronic contributions, the Lorenz ratio increases to more than 3 at 100 GPa. Although prior work revealed a departure from the predictions of the Wiedemann-Franz-Lorenz law in tungsten by 30% at ambient pressure [8], our work highlights the prominent role played by the lattice heat conduction in dictating the breakdown of this universal law by as much as 300% at pressures approaching 100 GPa.

Our results presented in this paper not only are of significance from the standpoint of a fundamental understanding of condensed matter, but also can be important from an applicative standpoint. For example, in microchips where metallic nanowires are highly sought-after for interconnect materials, the thermal transport properties are crucial for their design and implementation. The electrical resistivity of these wires increases through enhanced boundary scattering as their characteristic dimension is decreased, and the further miniaturization of integrated circuits, which mostly use Cu interconnects, increases approximately by an order of magnitude when the dimension is reduced down to 10 nm [12]. Therefore, when the characteristic size is comparable to the electronic  $\Lambda$ , the transport properties are highly influenced by size effects. As such, downscaling is beneficial for W nanowires as compared with the conventionally used Cu nanowires since the electronic  $\Lambda \sim 15.5$  nm as predicted from our parameter-free DFPT calculations for ambient conditions is much shorter than that in Cu (39 nm) [37]. We have shown that pressure has a negligible influence on the electron scattering rates (and therefore  $\Lambda$ ; see Figs. S12–S14) [63], and as such, our results could be significant for understanding the transport properties of the next generation of tungsten nanointerconnects, where, at the nanoscale, inherent strain effects might originate from interfaces and grain boundaries [66].

### III. CONCLUSIONS

In conclusion, by comprehensively investigating the responses of the electronic and phononic subsystems subjected to high pressures in tungsten, we have shown that the thermal transport transitions from an electron-dominated heat transfer (with  $\sim 70\%$  contribution of  $\kappa_e$  under ambient conditions) to a phonon-dominated heat transfer at elevated pressures (with up to  $\sim 70\%$  contribution to the total thermal conductivity from  $\kappa_p$  at 100 GPa). This is due to the fact that while  $\kappa_p$  increases monotonically with pressure,  $\kappa_e$  shows negligible variation with increasing pressures. We have ascribed this relative insensitivity of the electronic thermal transport to the intrinsic band structure in tungsten, which differs considerably from the band structure of other metals such as free-electron-like metals, where  $\kappa_e$  has a dramatic increase with pressure. The phonon contribution to the total thermal conductivity increases due to lattice stiffening leading to enhanced phonon group velocities and lifetimes with increasing pressures. Unique to tungsten, this enhanced lattice contribution can be prescribed to its characteristically isotropic and

degenerate phonon branches, which lead to reduced phonon-phonon scattering leading to the severe breakdown of the Wiedemann-Franz law, especially under extreme pressures.

### ACKNOWLEDGMENT

This work is supported by the Office of Naval Research, Grant No. N00014-21-1-2622.

### APPENDIX A: FIRST-PRINCIPLES CALCULATIONS OF ELECTRON-PHONON INTERACTIONS

The electron-phonon matrix elements are calculated utilizing the EPW (derived from “electron-phonon Wannier”) package [6] and the QUANTUM ESPRESSO (QE) package [67], which are used to perform the density functional perturbation theory (DFPT) calculations. The densely packed phonon and electron wave vectors (i.e.,  $\mathbf{q}$  and  $\mathbf{k}$ , respectively) in the Brillouin zone are crucial for the calculation of the Eliashberg function describing the spectral electron-phonon coupling strength, which is given as

$$\alpha_{\text{tr}}^2 F(\omega) = \frac{1}{N(\varepsilon_{\text{F}})} \sum_{\mathbf{q}j} \sum_{\mathbf{k}nm} |g_{\mathbf{k}+\mathbf{q}m,\mathbf{k}n}^{\mathbf{q}j}|^2 \delta(\hbar\omega - \hbar\omega_{\mathbf{q}j}) \times \delta(\varepsilon_{\mathbf{k}n} - \varepsilon_{\text{F}}) \delta(\varepsilon_{\mathbf{k}+\mathbf{q}m} - \varepsilon_{\text{F}}) \eta_{\mathbf{k}+\mathbf{q}m,\mathbf{k}n}, \quad (\text{A1})$$

where  $j$  stands for the branch index of  $\mathbf{q}$ ,  $N(\varepsilon_{\text{F}})$  denotes the density of states (DOS) of electrons at the Fermi level, and  $g_{\mathbf{k}+\mathbf{q}m,\mathbf{k}n}^{\mathbf{q}j}$  are the electron-phonon (e-p) matrix elements that quantify the scattering of an electron at the Fermi surface from the state  $|\mathbf{k}n\rangle$  to the state  $|\mathbf{k}+\mathbf{q}m\rangle$ . The efficiency factor,

$$\eta_{\mathbf{k}+\mathbf{q}m,\mathbf{k}n} = 1 - \frac{\mathbf{v}_{\mathbf{k}n} \cdot \mathbf{v}_{\mathbf{k}+\mathbf{q}m}}{|\mathbf{v}_{\mathbf{k}n}|^2}, \quad (\text{A2})$$

considers different scattering directions to account for the anisotropic behavior. The efficiency factor is dependent on the electron velocity  $\mathbf{v}_{\mathbf{k}n}$  and differentiates between the spectral function  $\alpha^2 F(\omega)$  and the transport spectral function.

The imaginary parts of the electron and phonon self-energies are calculated as [5,6]

$$\Sigma_{n\mathbf{k}}(\omega, T) = \sum_{mv} \int_{\text{BZ}} \frac{d\mathbf{q}}{\Omega_{\text{BZ}}} |g_{m\mathbf{n},v}(\mathbf{k}, \mathbf{q})|^2 \times \left[ \frac{N_{\mathbf{q},v}(T) + f_{m\mathbf{k}+\mathbf{q}}}{\omega - (\varepsilon_{m\mathbf{k}+\mathbf{q}} - \varepsilon_{\text{F}}) + \omega_{\mathbf{q},v} + i\delta} + \frac{N_{\mathbf{q},v}(T) + 1 - f_{m\mathbf{k}+\mathbf{q}}(T)}{\omega - (\varepsilon_{m\mathbf{k}+\mathbf{q}} - \varepsilon_{\text{F}}) - \omega_{\mathbf{q},v} + i\delta} \right], \quad (\text{A3})$$

$$\Pi_{\mathbf{q}v}(\omega, T) = 2 \sum_{mn} \int_{\text{BZ}} \frac{d\mathbf{k}}{\Omega_{\text{BZ}}} |g_{m\mathbf{n},v}(\mathbf{k}, \mathbf{q})|^2 \times \frac{f_{n\mathbf{k}}(T) - f_{m\mathbf{k}+\mathbf{q}}(T)}{\varepsilon_{m\mathbf{k}+\mathbf{q}} - \varepsilon_{n\mathbf{k}} - \omega - i\delta}, \quad (\text{A4})$$

where  $N_{\mathbf{q},v}$  is the Bose-Einstein distribution,  $f_{n\mathbf{k}}(T)$  is the Fermi-Dirac distribution at band  $n$ ,  $\delta$  is a small positive real parameter to avoid numerical instabilities and thus guarantee the correct analytical structure of the self-energies, and the integrals are extended over the Brillouin zone of volume  $\Omega_{\text{BZ}}$  [5,6].

For highly accurate calculation of Eq. (A1), dense  $\mathbf{q}$  and  $\mathbf{k}$  grids in the Brillouin zone are paramount. This is accomplished by the interpolation of the e-p matrix elements, the phonon modes, and the band energies from initial coarse grids of  $10 \times 10 \times 10$  and  $5 \times 5 \times 5$  to uniform grids of  $90 \times 90 \times 90$  and  $35 \times 35 \times 35$ , for electron and phonon wave-vector grids, respectively. The interpolation is achieved by employing maximally localized Wannier functions from the Bloch energy bands [40]. For these calculations, we use a Bachelet-Hamann-Schlüter-type (BHS-type) scalar relativistic, norm-conserving pseudopotential taken from the legacy QE pseudopotential (PP) table [68] with the Perdew-Zunger [local density approximation (LDA)] exchange-correlation functional and consider  $5d$  and  $6s$  bands with six electrons for tungsten. We implement a plane-wave cutoff of 1632.7 eV (120 Ry) for these calculations for a single body-centered-cubic unit cell of the metals.

## APPENDIX B: AB INITIO MD AND MACHINE LEARNING POTENTIAL FOR MD

We use diverse training data sets based on *ab initio* MD simulations to formulate interatomic potentials to be employed in our extensive classical MD simulations. For high accuracies, we note that we develop two different potentials: The first interatomic potential is specifically developed to capture the correct vibrational physics at ambient pressure across the 300–1100 K temperature range. The second interatomic potential is developed to perform MD simulations under high-pressure conditions (spanning 0–100 GPa).

All our *ab initio* MD simulations are performed using the QUANTUM ESPRESSO package [67]. For our first MLP, the atomic coordinates, forces, energies, and cell parameters are obtained by taking snapshots of the *ab initio* MD trajectories during finite-temperature simulations from ambient temperature to 1100 K. This is done to sample the configurational space as far as practicable since the predictive capability of the machine learning potential highly depends upon quality and diversity of training data set. The energy cutoff for plane-wave expansion and the energy convergence for the self-consistent field (SCF) are set to 25 Ry and  $10^{-6}$  a.u., respectively. We ensure that the choice of 25 Ry for the plane-wave energy does not influence our results by considering cutoffs in the range 25–125 Ry, which showed no change in the converged energies in our SCF calculations. Moreover, the agreement between the DFT-calculated phonon dispersion with 125 Ry as the plane-wave cutoff and the phonon dispersion calculated based on the MLP developed with our choice of 25 Ry for our *ab initio* MD suggests that the cutoff does not influence the lattice dynamics of tungsten in our classical MD simulations.

The Brillouin zone is sampled over a  $4 \times 4 \times 4$  Monkhorst-Pack mesh. Fermi-Dirac smearing is used to account for temperatures ranging from 300 to 1100 K. The cell parameters are allowed to relax in all of our *ab initio* MD simulations using the isobaric-isothermal ensemble. All *ab initio* MD simulations are performed on a  $2 \times 2 \times 2$  supercell. For the first potential, the pressure is fixed to zero for each simulation using a Parrinello-Rahman barostat [69], and temperature is held constant by using the rescaling technique for temperature-based simulations at 0 GPa. *Ab initio* MD

simulations were performed at various temperatures ranging from 300 to 1100 K to develop an interatomic potential that is accurate across the entire temperature range. For the second interatomic potential, the pressure is changed gradually from 0 to 100 GPa with a step of 10 GPa. A time step of 2 fs is used in all of our *ab initio* MD simulations. A total of 11 825 data sets are generated by *ab initio* simulations for the temperature-based machine learning potential. A set of 1000 data frames that were not included in the training data set is used as a validation data set to assess the accuracy of the model. For the second interatomic potential to describe thermal transport under high-pressure conditions, a total of 8000 data sets obtained are split into training as well as validation data sets. From this, 7200 data sets are used as the training data set, and 800 data frames that are not used in the training are used to infer the accuracy of the MLP as the validation data set.

For the purpose of accurately mapping the position space of atoms with their energy space, a deep learning framework (DEEPM) [70] is used to construct a deep potential–smooth edition (or DeepPot-SE) neural model by training the data set, which considers both radial and angular components to produce the descriptors for training. We utilize the DEEPM package’s deep learning framework TENSORFLOW for training and testing the machine learning interatomic potential used in our MD simulations performed with the Large-Scale Atomic/Molecular Massively Parallel Simulator (LAMMPS) package [71]. The cutoff radius is set to be 6 Å, and the descriptors decay from 0.5 to 6 Å to remove the discontinuity introduced by the cutoff. The neural architecture consists of two neural networks: one to convert the atomic coordinates to descriptors and the other to map the descriptors to their respective atomic energies. The former is known as the embedding network, and the latter is known as the fitting network. The embedding network consists of three hidden layers with sizes of 25, 50, and 100 following residual-network-like (ResNet-like) architecture [72]. The fitting network consists of three hidden layers with 240 neurons each. The cost function optimization is achieved by using the adaptive moment estimation (ADAM)–stochastic gradient descent approach. The learning rate is varied from  $10^{-3}$  to  $10^{-8}$  with an exponential decay in 1 000 000 steps for our temperature-based model and 10 000 000 steps for our pressure-based model. The prefactors of energies and forces are set as  $P_e^{\text{start}} = 0.01$ ,  $P_f^{\text{start}} = 1000$ ,  $P_e^{\text{limit}} = 1$ , and  $P_f^{\text{limit}} = 1$ , respectively.

The training accuracy increases with the number of steps. For the temperature-based model, training root-mean-square errors (RMSEs) of  $1.17 \times 10^{-3}$  eV/atom and  $8.02 \times 10^{-3}$  eV/Å were achieved for energy and force, respectively. A test data set of 1000 frames is used to infer the accuracy of the trained potential. The test RMSEs of  $2.25 \times 10^{-3}$  eV/atom for energy and  $2.21 \times 10^{-2}$  eV/Å for force were obtained indicating the accuracy of our MLP. Similarly, for the pressure-based model training RMSEs of  $1.19 \times 10^{-3}$  eV/atom and  $4.32 \times 10^{-3}$  eV/Å were achieved for energy and force, respectively. A test data set of 800 frames is used to infer the accuracy of the trained potential. The test RMSEs of  $1.89 \times 10^{-3}$  eV/atom for energy and  $5.72 \times 10^{-3}$  eV/Å for force were obtained indicating the high accuracy of our MLP.

For our validation MD runs the time step is set as 1.0 fs, and the temperature and pressure are controlled using a



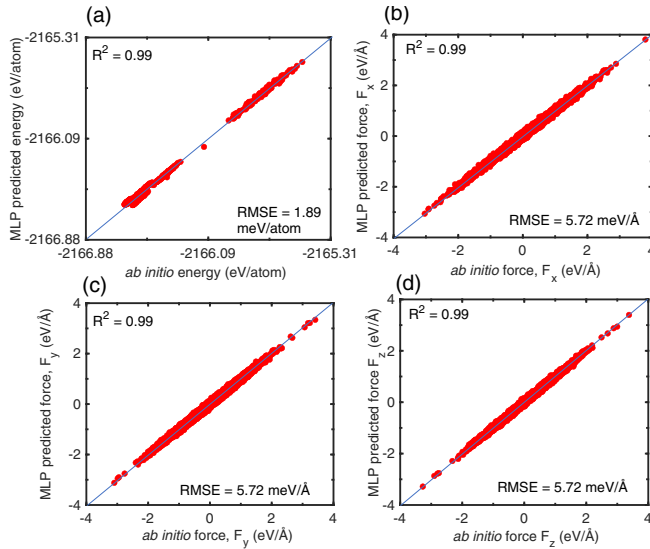


FIG. 6. Comparison of (a) energies and (b)–(d) forces obtained from our MLP MD simulations and *ab initio* MD for tungsten at 300 K. The low RMSE values, along with an  $R^2$  value of unity, indicate an excellent agreement between our MLP and *ab initio* MD simulations.

Nosé-Hoover thermostat and barostat, respectively [73]. The damping parameters were set to be 0.1 and 1 ps for the thermostat and barostat, respectively. Periodic boundary conditions are used in all directions for all simulations. To verify the accuracy of our MLPs, we compare the energies and forces we obtain with our MLP-MD simulations and *ab initio* MD simulations in Fig. 6. The great agreement between the two methods (with the low root-mean-square errors and  $R^2$  values close to 1) validates our potential and training procedure.

### APPENDIX C: GREEN-KUBO AND SPECTRAL ENERGY DENSITY CALCULATIONS

The MLPs are used with the GK formalism to determine the phonon thermal conductivity of tungsten, which is related to the heat current autocorrelation function (HCACF) expressed as

$$\kappa_{x,y,z} = \frac{1}{VK_B T^2} \int_0^\infty \langle J_{x,y,z}(0) J_{x,y,z}(t) \rangle dt, \quad (\text{C1})$$

where  $K_B$ ,  $T$ ,  $V$ , and  $t$  are the Boltzmann constant, temperature, volume, and time, respectively, and  $\langle J_{x,y,z}(0) J_{x,y,z}(t) \rangle$  is

the HCACF component along the  $x$ ,  $y$ , or  $z$  directions. The lattice thermal conductivities are calculated at various temperatures and pressures for our tungsten computational domains. Firstly, the energies of our computational domains are minimized based on the conjugate gradient approach, and then the cells are relaxed under the  $N$ - $P$ - $T$  ensemble (where the number of atoms, pressure, and temperature are held constant) for 1 ns with a target temperature and a pressure of 0 bars. The system is then relaxed under the  $N$ - $V$ - $T$  ensemble for another 1 ns. Finally, the  $N$ - $V$ - $E$  ensemble is used to collect the heat current data for the calculation of the lattice thermal conductivity according to Eq. (C1).

We determine the phonon lifetimes of our tungsten structures through the calculation of the SED in our MD simulations. The SED is obtained as a function of wave vector  $\mathbf{q}$  and frequency  $\omega$ , which is given as [64]

$$\Phi(\mathbf{q}, \omega) = \frac{1}{4\pi \tau N_T} \sum_j \sum_a^A m_a \left| \int_0^\tau \sum_{n_{x,y,z}}^{N_T} \dot{v}_j \left( \begin{matrix} n_{x,y,z} \\ a \end{matrix}; t \right) \times \exp \left[ i\mathbf{q} \cdot \mathbf{r} \left( \begin{matrix} n_{x,y,z} \\ 0 \end{matrix} \right) - i\omega t \right] dt \right|^2, \quad (\text{C2})$$

where  $\tau$  represents the total duration of the simulation,  $j$  corresponds to the Cartesian direction,  $n_{x,y,z}$  refers to a unit cell in the crystal structure,  $N_T$  represents the total number of unit cells in the crystal,  $a$  denotes the label of an atom within a specific unit cell,  $A$  is the atomic number in the unit cell, and  $m_a$  signifies the mass of atom  $a$  in the unit cell. The term  $\dot{v}_j$  represents the velocity of the atom labeled as  $a$  in the  $n$ th unit cell along the  $j$  direction at time  $t$ . Additionally,  $\mathbf{r}$  refers to the equilibrium position of each unit cell.

To perform our SED calculations, we create a supercell with dimensions of  $100 \times 4 \times 4$  for our tungsten structures. For the equilibration of our supercell structure, we initially employ the Nosé-Hoover thermostat and barostat (i.e., the  $N$ - $P$ - $T$  ensemble) [73], where the number of particles, pressure, and temperature of the system are kept constant at the desired pressure (0 or 80 GPa) for 2 ns with a time step of 0.5 fs. After completing the  $N$ - $P$ - $T$  integration, we continue the equilibration process under the  $N$ - $V$ - $T$  ensemble, where both the volume and temperature are held constant for an additional 2 ns. To collect the necessary data for our SED calculation, we extract the velocities and positions of each atom using the microcanonical ( $N$ - $V$ - $E$ ) ensemble for a period of 1.5 ns.

[1] C. Kittel, *Introduction to Solid State Physics*, 6th ed. (Wiley, New York, 1986).  
 [2] L. Lorenz, Ueber das Leitungsvermögen der Metalle für Wärme und Electricität, *Ann. Phys. (Berlin)* **249**, 582 (1881).  
 [3] R. Franz and G. Wiedemann, Ueber die Wärme-Leitungsfähigkeit der Metalle, *Ann. Phys. Chem.* **165**, 497 (1853).  
 [4] Z. Tong, S. Li, X. Ruan, and H. Bao, Comprehensive first-principles analysis of phonon thermal conductivity and electron-phonon coupling in different metals, *Phys. Rev. B* **100**, 144306 (2019).

[5] J. Noffsinger, F. Giustino, B. D. Malone, C.-H. Park, S. G. Louie, and M. L. Cohen, EPW: A program for calculating the electron-phonon coupling using maximally localized Wannier functions, *Comput. Phys. Commun.* **181**, 2140 (2010).  
 [6] S. Poncé, E. Margine, C. Verdi, and F. Giustino, EPW: Electron-phonon coupling, transport and superconducting properties using maximally localized Wannier functions, *Comput. Phys. Commun.* **209**, 116 (2016).  
 [7] A. Jain and A. J. H. McGaughey, Thermal transport by phonons and electrons in aluminum, silver, and gold from first principles, *Phys. Rev. B* **93**, 081206(R) (2016).

- [8] Y. Chen, J. Ma, and W. Li, Understanding the thermal conductivity and Lorenz number in tungsten from first principles, *Phys. Rev. B* **99**, 020305(R) (2019).
- [9] M. Cox, Thermal and electrical conductivities of tungsten and tantalum, *Phys. Rev.* **64**, 241 (1943).
- [10] J. F. Goff, Lorenz number of chromium, *Phys. Rev. B* **1**, 1351 (1970).
- [11] W. Steinhögl, G. Steinlesberger, M. Perrin, G. Scheinbacher, G. Schindler, M. Traving, and M. Engelhardt, Tungsten interconnects in the nano-scale regime, *Microelectron. Eng.* **82**, 266 (2005).
- [12] D. Gall, Electron mean free path in elemental metals, *J. Appl. Phys.* **119**, 085101 (2016).
- [13] D. Gall, The search for the most conductive metal for narrow interconnect lines, *J. Appl. Phys.* **127**, 050901 (2020).
- [14] P. F. McMillan, New materials from high-pressure experiments, *Nat. Mater.* **1**, 19 (2002).
- [15] D. U. Gubser and A. W. Webb, High-pressure effects on the superconducting transition temperature of aluminum, *Phys. Rev. Lett.* **35**, 104 (1975).
- [16] G. Profeta, C. Franchini, N. N. Lathiotakis, A. Floris, A. Sanna, M. A. L. Marques, M. Lüders, S. Massidda, E. K. U. Gross, and A. Continenza, Superconductivity in lithium, potassium, and aluminum under extreme pressure: A first-principles study, *Phys. Rev. Lett.* **96**, 047003 (2006).
- [17] J. Hamlin, Superconductivity in the metallic elements at high pressures, *Phys. C (Amsterdam)* **514**, 59 (2015).
- [18] D. A. Dalton, W.-P. Hsieh, G. T. Hohensee, D. G. Cahill, and A. F. Goncharov, Effect of mass disorder on the lattice thermal conductivity of MgO periclase under pressure, *Sci. Rep.* **3**, 2400 (2013).
- [19] B. Chen, W.-P. Hsieh, D. G. Cahill, D. R. Trinkle, and J. Li, Thermal conductivity of compressed H<sub>2</sub>O to 22 GPa: A test of the Leibfried-Schlömann equation, *Phys. Rev. B* **83**, 132301 (2011).
- [20] W.-P. Hsieh, M. D. Losego, P. V. Braun, S. Shenogin, P. Keblinski, and D. G. Cahill, Testing the minimum thermal conductivity model for amorphous polymers using high pressure, *Phys. Rev. B* **83**, 174205 (2011).
- [21] G. T. Hohensee, M. R. Fellingner, D. R. Trinkle, and D. G. Cahill, Thermal transport across high-pressure semiconductor-metal transition in Si and Si<sub>0.991</sub>Ge<sub>0.009</sub>, *Phys. Rev. B* **91**, 205104 (2015).
- [22] G. T. Hohensee, R. B. Wilson, and D. G. Cahill, Thermal conductance of metal–diamond interfaces at high pressure, *Nat. Commun.* **6**, 6578 (2015).
- [23] W.-P. Hsieh, A. S. Lyons, E. Pop, P. Keblinski, and D. G. Cahill, Pressure tuning of the thermal conductance of weak interfaces, *Phys. Rev. B* **84**, 184107 (2011).
- [24] R. B. Wilson, B. A. Apgar, W.-P. Hsieh, L. W. Martin, and D. G. Cahill, Thermal conductance of strongly bonded metal-oxide interfaces, *Phys. Rev. B* **91**, 115414 (2015).
- [25] L. Lindsay, D. A. Broido, J. Carrete, N. Mingo, and T. L. Reinecke, Anomalous pressure dependence of thermal conductivities of large mass ratio compounds, *Phys. Rev. B* **91**, 121202(R) (2015).
- [26] D. A. Broido, L. Lindsay, and A. Ward, Thermal conductivity of diamond under extreme pressure: A first-principles study, *Phys. Rev. B* **86**, 115203 (2012).
- [27] N. K. Ravichandran and D. Broido, Non-monotonic pressure dependence of the thermal conductivity of boron arsenide, *Nat. Commun.* **10**, 827 (2019).
- [28] A. Giri, J. T. Gaskins, L. Li, Y.-S. Wang, O. V. Prezhdo, and P. E. Hopkins, First-principles determination of the ultrahigh electrical and thermal conductivity in free-electron metals via pressure tuning the electron-phonon coupling factor, *Phys. Rev. B* **99**, 165139 (2019).
- [29] P. Karna and A. Giri, Effect of intense laser irradiation on the thermal transport properties of metals, *Phys. Rev. B* **107**, 094301 (2023).
- [30] A. Hasegawa, T. Yagi, and K. Ohta, Combination of pulsed light heating thermoreflectance and laser-heated diamond anvil cell for in-situ high pressure-temperature thermal diffusivity measurements, *Rev. Sci. Instrum.* **90**, 074901 (2019).
- [31] M. I. Kaganov, Relaxation between electrons and the crystalline lattice, *Sov. Phys. JETP* **4**, 173 (1957).
- [32] S. I. Anisimov, B. L. Kapeliovich, and T. L. Perelman, Electron emission from metal surfaces exposed to ultrashort laser pulses, *Zh. Eksp. Teor. Fiz.* **66**, 375 (1974).
- [33] P. B. Allen, T. P. Beaulac, F. S. Khan, W. H. Butler, F. J. Pinski, and J. C. Swihart, dc transport in metals, *Phys. Rev. B* **34**, 4331 (1986).
- [34] P. B. Allen, Theory of thermal relaxation of electrons in metals, *Phys. Rev. Lett.* **59**, 1460 (1987).
- [35] P. B. Allen, Empirical electron-phonon  $\lambda$  values from resistivity of cubic metallic elements, *Phys. Rev. B* **36**, 2920 (1987).
- [36] Z. Lin, L. V. Zhigilei, and V. Celli, Electron-phonon coupling and electron heat capacity of metals under conditions of strong electron-phonon nonequilibrium, *Phys. Rev. B* **77**, 075133 (2008).
- [37] A. M. Brown, R. Sundararaman, P. Narang, W. A. Goddard, and H. A. Atwater, Nonradiative plasmon decay and hot carrier dynamics: Effects of phonons, surfaces, and geometry, *ACS Nano* **10**, 957 (2016).
- [38] X. Zhang, S. Li, A. Wang, and H. Bao, Pressure-dependent thermal conductivity in Al, W, and Pt: Role of electrons and phonons, *Phys. Rev. B* **106**, 094313 (2022).
- [39] T. Bazhironov, J. Noffsinger, and M. L. Cohen, Superconductivity and electron-phonon coupling in lithium at high pressures, *Phys. Rev. B* **82**, 184509 (2010).
- [40] N. Marzari, A. A. Mostofi, J. R. Yates, I. Souza, and D. Vanderbilt, Maximally localized Wannier functions: Theory and applications, *Rev. Mod. Phys.* **84**, 1419 (2012).
- [41] S. Li, Z. Tong, X. Zhang, and H. Bao, Thermal conductivity and Lorenz ratio of metals at intermediate temperatures with mode-level first-principles analysis, *Phys. Rev. B* **102**, 174306 (2020).
- [42] S. Wen, J. Ma, A. Kundu, and W. Li, Large lattice thermal conductivity, interplay between phonon-phonon, phonon-electron, and phonon-isotope scatterings, and electrical transport in molybdenum from first principles, *Phys. Rev. B* **102**, 064303 (2020).
- [43] A. Giri, M. Tokina, O. Prezhdo, and P. Hopkins, Electron-phonon coupling and related transport properties of metals and intermetallic alloys from first principles, *Mater. Today Phys.* **12**, 100175 (2020).
- [44] A. Giri, P. Karna, and P. E. Hopkins, Exceptionally enhanced thermal conductivity of aluminum driven by extreme

- pressures: A first-principles study, *J. Phys. Chem. Lett.* **13**, 10918 (2022).
- [45] A. J. H. McGaughey, A. Jain, H.-Y. Kim, and B. Fu, Phonon properties and thermal conductivity from first principles, lattice dynamics, and the Boltzmann transport equation, *J. Appl. Phys.* **125**, 011101 (2019).
- [46] L. Lindsay, First principles Peierls-Boltzmann phonon thermal transport: A topical review, *Nanoscale Microscale Thermophys. Eng.* **20**, 67 (2016).
- [47] T. Feng and X. Ruan, Quantum mechanical prediction of four-phonon scattering rates and reduced thermal conductivity of solids, *Phys. Rev. B* **93**, 045202 (2016).
- [48] T. Feng, L. Lindsay, and X. Ruan, Four-phonon scattering significantly reduces intrinsic thermal conductivity of solids, *Phys. Rev. B* **96**, 161201(R) (2017).
- [49] T. Feng and X. Ruan, Four-phonon scattering reduces intrinsic thermal conductivity of graphene and the contributions from flexural phonons, *Phys. Rev. B* **97**, 045202 (2018).
- [50] N. K. Ravichandran and D. Broido, Unified first-principles theory of thermal properties of insulators, *Phys. Rev. B* **98**, 085205 (2018).
- [51] F. Tian, B. Song, X. Chen, N. K. Ravichandran, Y. Lv, K. Chen, S. Sullivan, J. Kim, Y. Zhou, T.-H. Liu, M. Goni, Z. Ding, J. Sun, G. A. G. U. Gamage, H. Sun, H. Ziyae, S. Huyan, L. Deng, J. Zhou, A. J. Schmidt *et al.*, Unusual high thermal conductivity in boron arsenide bulk crystals, *Science* **361**, 582 (2018).
- [52] P. Korotaev, I. Novoselov, A. Yanilkin, and A. Shapeev, Accessing thermal conductivity of complex compounds by machine learning interatomic potentials, *Phys. Rev. B* **100**, 144308 (2019).
- [53] R. Li, E. Lee, and T. Luo, A unified deep neural network potential capable of predicting thermal conductivity of silicon in different phases, *Mater. Today Phys.* **12**, 100181 (2020).
- [54] S. Faraji, S. M. V. Allaei, and M. Amsler, Thermal conductivity of  $\text{CaF}_2$  at high pressure, *Phys. Rev. B* **103**, 134301 (2021).
- [55] B. Mortazavi, E. V. Podryabinkin, I. S. Novikov, S. Roche, T. Rabczuk, X. Zhuang, and A. V. Shapeev, Efficient machine-learning based interatomic potentials for exploring thermal conductivity in two-dimensional materials, *J. Phys.: Mater.* **3**, 02LT02 (2020).
- [56] H. Babaei, R. Guo, A. Hashemi, and S. Lee, Machine-learning-based interatomic potential for phonon transport in perfect crystalline Si and crystalline Si with vacancies, *Phys. Rev. Mater.* **3**, 074603 (2019).
- [57] Y.-B. Liu, J.-Y. Yang, G.-M. Xin, L.-H. Liu, G. Csányi, and B.-Y. Cao, Machine learning interatomic potential developed for molecular simulations on thermal properties of  $\beta\text{-Ga}_2\text{O}_3$ , *J. Chem. Phys.* **153**, 144501 (2020).
- [58] S. Wyant, A. Rohskopf, and A. Henry, Machine learned interatomic potentials for modeling interfacial heat transport in Ge/GaAs, *Comput. Mater. Sci.* **200**, 110836 (2021).
- [59] E. Minamitani, M. Ogura, and S. Watanabe, Simulating lattice thermal conductivity in semiconducting materials using high-dimensional neural network potential, *Appl. Phys. Express* **12**, 095001 (2019).
- [60] A. Larose and B. N. Brockhouse, Lattice vibrations in tungsten at 22 °C studied by neutron scattering, *Can. J. Phys.* **54**, 1819 (1976).
- [61] W. H. Butler and R. K. Williams, Electron-phonon interaction and lattice thermal conductivity, *Phys. Rev. B* **18**, 6483 (1978).
- [62] Y. Chen, J. Ma, S. Wen, and W. Li, Body-centered-cubic structure and weak anharmonic phonon scattering in tungsten, *npj Comput. Mater.* **5**, 98 (2019).
- [63] See Supplemental Material at <http://link.aps.org/supplemental/10.1103/PhysRevMaterials.7.115001> for details regarding the validation of the machine learning potential, the convergence test for the calculations of the electron-phonon coupling matrix, the electronic structure and properties calculations for tungsten, and further details of the equilibrium molecular dynamics simulations, which also includes Refs. [8,74–77].
- [64] J. A. Thomas, J. E. Turney, R. M. Iutzi, C. H. Amon, and A. J. H. McGaughey, Predicting phonon dispersion relations and lifetimes from the spectral energy density, *Phys. Rev. B* **81**, 081411(R) (2010).
- [65] P. C. Howell, Comparison of molecular dynamics methods and interatomic potentials for calculating the thermal conductivity of silicon, *J. Chem. Phys.* **137**, 224111 (2012).
- [66] P. Zheng and D. Gall, The anisotropic size effect of the electrical resistivity of metal thin films: Tungsten, *J. Appl. Phys.* **122**, 135301 (2017).
- [67] P. Giannozzi, S. Baroni, N. Bonini, M. Calandra, R. Car, C. Cavazzoni, D. Ceresoli, G. L. Chiarotti, M. Cococcioni, I. Dabo, A. D. Corso, S. de Gironcoli, S. Fabris, G. Fratesi, R. Gebauer, U. Gerstmann, C. Gougoussis, A. Kokalj, M. Lazzeri, L. Martin-Samos *et al.*, QUANTUM ESPRESSO: A modular and open-source software project for quantum simulations of materials, *J. Phys.: Condens. Matter* **21**, 395502 (2009).
- [68] G. B. Bachelet, D. R. Hamann, and M. Schlüter, Pseudopotentials that work: From H to Pu, *Phys. Rev. B* **26**, 4199 (1982).
- [69] R. Martoňák, A. Laio, and M. Parrinello, Predicting crystal structures: The Parrinello-Rahman method revisited, *Phys. Rev. Lett.* **90**, 075503 (2003).
- [70] H. Wang, L. Zhang, J. Han, and E. Weinan, DeePMD-kit: A deep learning package for many-body potential energy representation and molecular dynamics, *Comput. Phys. Commun.* **228**, 178 (2018).
- [71] S. Plimpton, Fast parallel algorithms for short-range molecular dynamics, *J. Comput. Phys.* **117**, 1 (1995).
- [72] K. He, X. Zhang, S. Ren, and J. Sun, Deep residual learning for image recognition, in *Proceedings of the IEEE Conference on Computer Vision and Pattern Recognition* (IEEE, Piscataway, NJ, 2016), pp. 770–778.
- [73] W. G. Hoover, Canonical dynamics: Equilibrium phase-space distributions, *Phys. Rev. A* **31**, 1695 (1985).
- [74] F. H. Featherston and J. R. Neighbours, Elastic constants of tantalum, tungsten, and molybdenum, *Phys. Rev.* **130**, 1324 (1963).
- [75] J. D. Noffsinger, The electron-phonon interaction from first principles, Ph.D. thesis, University of California, Berkeley, 2011, <https://escholarship.org/uc/item/9v2759zn>.
- [76] F. Giustino, M. L. Cohen, and S. G. Louie, Electron-phonon interaction using Wannier functions, *Phys. Rev. B* **76**, 165108 (2007).
- [77] N. W. Ashcroft, Putting the squeeze on lithium, *Nature (London)* **419**, 569 (2002).